The 4th International Workshop on Ultrasonic and Advanced Methods for Nondestructive Testing and Material Characterization, June 19, 2006 at UMass Dartmouth, N. Dartmouth, MA – Proceedings published in www.ndt.net

Damage and defect inspection with terahertz waves

Albert Redo-Sanchez, Nicholas Karpowicz, Jingzhou Xu, and X.-C. Zhang

Rensselaer Polytechnic Institute, 110 8th St, Troy, NY 12180

Email: zhangxc@rpi.edu, redosa@rpi.edu

Abstract- We present recent results in applying pulsed and continuous-wave (CW) terahertz (THz) imaging and sensing techniques on damage and defect assessment in insulating foam and carbon fiber materials. The comparison between the optical inspections versus the THz image of the defects in the foam shows a very good agreement. For the carbon fiber samples, both THz imaging at 0.6 THz and time-domain data are used to evaluate the degree of heat damage. The carbon fiber has a polarization dependent reflectivity in the THz frequency range, which can be related to burn damage level.

Introduction

In the past years, terahertz (THz) technology has received more interest and attention because of its unique properties and capabilities that make it very attractive as a non-destructive evaluation (NDE) tool. The THz frequency region represents an important intersection between spatial resolution and penetration depth and many dry, non-metallic materials show little THz absorption which allows imaging their internal structure with THz. These materials (such as plastics, ceramics, clothes, etc) are usually also transparent to microwave radiation, but terahertz radiation has the potential for a higher spatial resolution due to its shorter wavelength. THz radiation is non-ionizing and presents a low risk to biological tissue, which makes THz imaging also very attractive for biological applications. On the other hand, THz radiation cannot penetrate metal objects or materials with significant water content.

There are basically two types of THz radiation technology: pulsed [1] and continuous-wave [2-5] (CW). A pulsed system is based on the use of electromagnetic wave pulses in the range of picosecond duration. This pulse is sent to a sample and is the resulting waveform is coherently recorded in time-domain. This waveform can be analyzed later in frequency by means of a Fourier Transform. CW systems work at single frequencies and do not provide spectroscopic information but they can be faster, more compact and simpler to operate.

In the past years, the inspection of the sprayed-on foam insulation (SOFI) used on the external tank of the Space Shuttle has been a major driving force to use THz technologies as a NDE tool. SOFI is a good subject for THz imaging because it has a low absorption coefficient and index of refraction in this range [6-7]. The samples, provided by Lockheed Martin Space Systems and NASA Marshall Flight Center, are sprayed layer-by-layer onto an aluminum substrate. Both pulsed and CW techniques can be used to image the samples. So far, CW systems are simpler and faster than pulsed system and quite a few results have been published already [8-9]. The effort to implement THz as an effective NDE tools continues and, indeed, THz technology is in NASA's phase 4, which means that THz imaging may become space certificated and implemented as a standard verification stage in the inspection procedure.

Beside the SOFI inspection, THz technology has also great potential in the inspection of other materials. In this paper the inspection of carbon fiber composites is explored. Carbon fiber composites are widely used in aerospace industry and their use requires technologies that are able to differentiate between safe and unsafe materials according to manufacturing tolerance or damage suffered in their use. In particular, the damaged caused by heat is the interest of study for the carbon fiber materials. Actually, the evaluation of such damage is performed by visual and destructive techniques, thus, the availability of a NDE tool is very attractive. In more detail, the carbon fiber samples inspected in this paper are used as a structural component in the fuselage of an aircraft.

The applications reported in this paper use different THz technologies and setups. In particular, the SOFI foam inspection is performed by CW systems while the carbon fiber and electrical insulator rods use both CW and pulsed wave techniques for the inspection. As for the CW systems, the sources are Gunn diodes and a gas THz laser. Gunn diodes are particularly attractive at sub-THz range because of its compactness and simple operation but are difficult to obtain them commercially above 0.8 THz. A THz gas uses a CO_2 laser to pump a gas cavity filled with the proper gas at the proper pressure. The THz gas laser offers several lines from 1 THz to 6 THz by changing the pumped gas. The detectors used are either Schottky diodes or pyroelectric. Schottky diodes are narrowband and have a very fast response and are used along the Gunn diodes while pyroelectric are broadband and slow and are used with the THz gas laser.

Measurements

The CW systems use Gunn diodes at 0.2 and 0.38 THz and the THz gas laser (Coherent SIFIR-50) at 1.63 THz with a power of 20 mW, 5 mW, and 180 mW respectively. Schottky diodes are used at 0.2 and 0.38 THz, and a pyroelectric at 1.63 THz. The beam is focused by aspherical (hyperbolic) lenses and three geometries can be implemented: transmission, normal reflection, and small angle reflection. The spot size is diffraction limited and it goes from 2.7 mm at 0.2 THz to 0.5 mm at 1.63 THz. Because all these systems are point emitters and receivers, the image is obtained by raster scan of the sample [8-9].

The THz time-domain system used to inspect the carbon fiber samples implements a Ti:Sapphire oscillator (Spectra-Physics Mai Tai), which produces pulses of 800 nm central wavelength, 80 fs duration, and 80 MHz repetition rate with an average power of 800 mW. It uses a p-type InAs wafer as emitter and a ZnTe crystal as detector via electro-optical rectification [10]. The measurements are performed in N_2 environment to remove the effects of water vapor absorption and in small angle reflection geometry.

SOFI samples are imaged with CW systems at 0.2 and 0.38 THz in normal reflection geometry. CW systems in normal reflection geometry show a common problem related to the generation of an interference pattern due to the interference between the incoming beam and reflected beams from the sample, lens and other surfaces. In order to reduce such effect, the system incorporates a compensating mirror with the intention to send part of radiation reflected from the beam splitter again to the detector in order to cancel the reflection coming from the lens, which is the main reflective surface besides the sample itself. One SOFI sample is imaged in order to check the difference in resolution and dynamic range. 0.38 THz images are expected to give a better resolution but the power available is less and the absorption is higher, which may cause a worse image quality. Another SOFI sample is imaged at 0.2 THz with the intention to

identify all defects and later slice it in small section to verify visually whether the defects are real or not. Also, this will allow verifying if some important defect was present buy not detected.

Carbon fiber-based materials are conductive and therefore exhibit a high THz reflectivity. As a result, the measurements are uniformly performed in a reflection imaging geometry, which has the advantage of more accurately simulating the type of measurement that could be performed in a real-world setting. The majority of carbon fiber materials have polarization-dependent reflectivity in the THz frequency range, which may provide the mechanism to evaluate the damage degree because the heat may change the local reflectivity by resin alteration and/or fiber distortion.

Results

SOFI foam

The defects to be detected within a SOFI sample can be mainly divided in two types: voids and delaminations. Voids are basically air bubbles trapped inside the foam during the manufacturing process. A delamination is a detachment of two adjacent sprayed layers and is the less common defects. Voids appear as dark shapes with light interiors, corresponding to the scattering and interference at the edge of the feature and enhanced transmission due to the lack of material in the interior, while a delamination appears as a dark line corresponding also to the scattering of the air layer.

Fig. 1 shows the results of imaging a SOFI sample at 0.2 and 0.38 THz. The resolution is better at 0.38 THz but the noise is also higher. This is caused because the power and dynamic range at 0.38 is lower and the absorption is higher. For instance, the absorption at 0.2 THz is ~2 dB/inch, while the absorption at 0.38 THz is ~3 dB/inch. The thickness of the sample is 4", resulting in a total attenuation of 24 dB, while the dynamic range of the system is ~32 dB. The dynamic range at 0.2 is ~35 dB, which is similar to the 0.38 THz system but the total attenuation is much smaller, which is 16 dB. The interference pattern is also more remarkable at 0.38 THz than at 0.2 THz again because of the smaller dynamic range. However, at 0.38 THz the image is good enough to identify most of defects and may be a viable option to identify small defects located in thin samples (<4 inches).

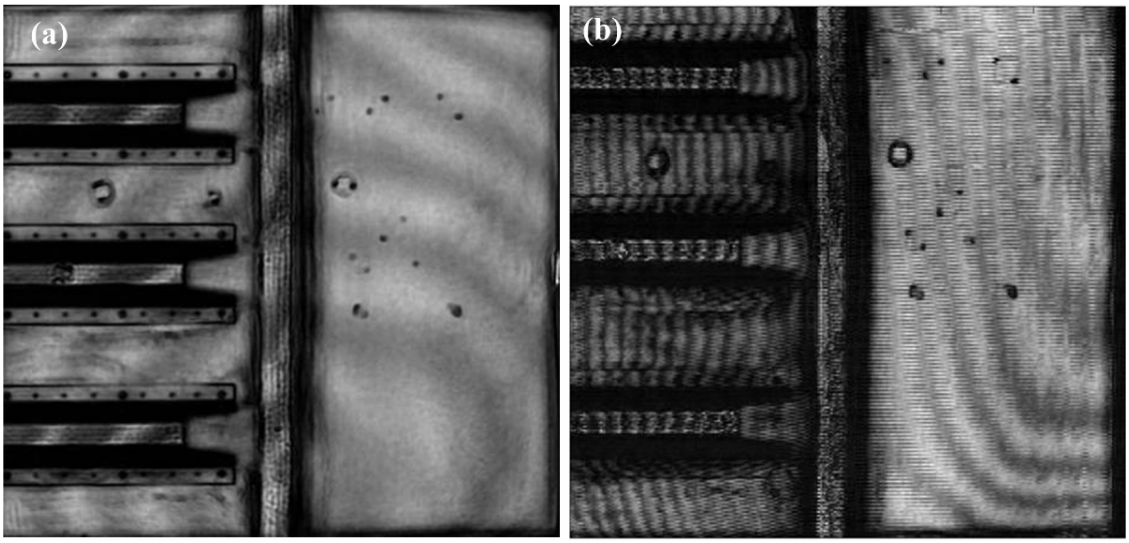

Fig. 1. THz image comparison between 0.2 THz (a) and 0.4 THz (b). The resolution at 0.4 THz is better but the signal is weaker and the interference pattern is more remarkable.

Fig. 2 and Fig. 3 show the THz image and the visual inspection of the defects respectively of another SOFI sample, which is between 6" to 8" thick. The THz image was obtained first and then the sample was sliced in sections of 1 cm thick in order to verify if the apparent defect in the THz image was real or not and if the structure seen in the image resembled the structure of the actual defect. The results show a complete match between what is seen in the THz image and what is seen in the visual inspection. In particular, 7 major defects were caught including delaminations (defects #2 and #3) and voids (others).

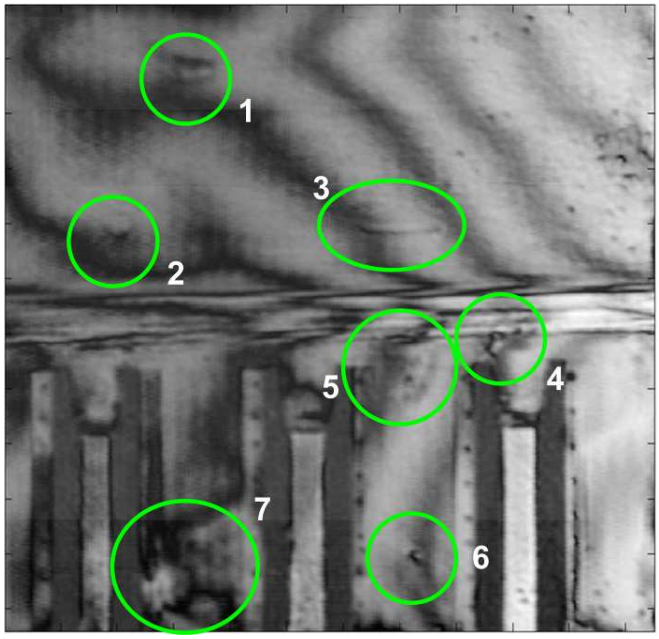

Fig. 2. THz image at 0.2 THz with some identified defects.

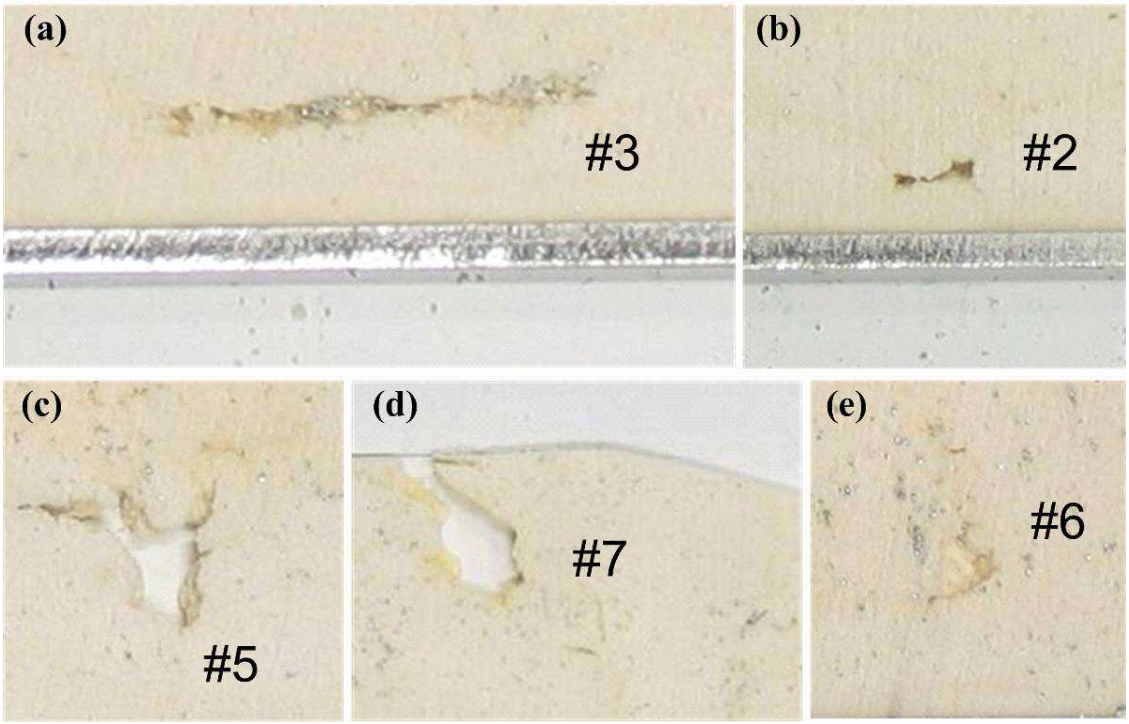

Fig. 3. Optical appearance of the defects obtained in Fig. 2. Defect #2 and #3 are delaminations while the other are voids.

In order to better understand the origin of the pattern seen in all pictures but more remarkable at 0.38 THz, a mathematical model is outlined in Fig. 4. The radiation emitted by the source goes to the sample and crosses a beam splitter and a lens. Part of the radiation is reflected from the beam splitter to the compensating mirror and another part is reflected by the lens. The reflection from the sample is collected again by the lens and reflected to the detector by the beam splitter. The radiation from the sample is composed by to reflections: one is from the substrate and the other is from the very first surface of the sample. All these beams are expected to interfere with each other when they reach the detector.

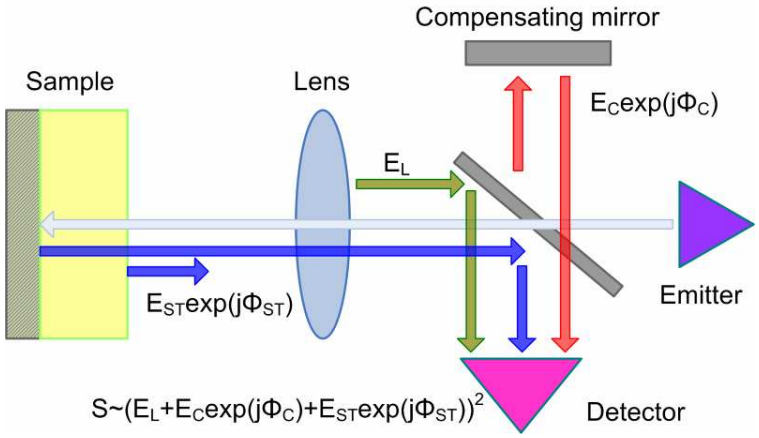

Fig. 4. Interference generation model. Three main beams arrive to the detector, the reflection from the lens, the reflection from the compensating mirror and the reflection

from the sample, which is composed by the reflection of the substrate and the reflection from the first substrate.

The signal of the detector (S) is proportional to the power, which is composed by the different beams with their respective phases arriving to the detector:

$$\begin{aligned} S = & E_L^2 + E_C^2 + E_S^2 + E_F^2 + \\ & + 2E_L E_C \cos(\phi_C) + 2E_L E_S \cos(\phi_S) + 2E_L E_F \cos(\phi_F) + \\ & + 2E_C E_S \cos(\phi_C - \phi_S) + 2E_C E_F \cos(\phi_C - \phi_F) + \\ & + 2E_S E_F \cos(\phi_S - \phi_F) \end{aligned} \tag{1}$$

Where E_0 is the output of the source, E_L the reflection from the lens, $E_C \exp(j\phi_C)$ the reflection from the compensating mirror (with a different phase respect the reflection from the lens), $E_{ST} \exp(j\phi_{ST}) = E_S \exp(j\phi_S) + E_F \exp(j\phi_F)$ is the reflection from the sample (composed by the reflection of the substrate E_S and the first surface E_F). The multiple reflections inside the sample are not considered. If the compensating mirror is not present, $E_C = 0$ and equation (1) turns into:

$$S^2 = E_L^2 + E_S^2 + E_F^2 + 2E_L E_S \cos(\phi_S) + 2E_L E_F \cos(\phi_F) + 2E_S E_F \cos(\phi_S - \phi_F) \tag{2}$$

This equation shows that there will be three interference patterns: the two reflections from the sample and each of these reflections with the reflection from the lens. There is not much control over this pattern because they are generated basically by the sample.

Now, if the compensating mirror is used and is set to cancel the background signal when no sample is present in front of the system in such a way that:

$$S^2 = E_L^2 \left(1 + \alpha^2 + 2\alpha \cos(\phi_C)\right) \approx 0 \tag{3}$$

$\alpha = E_C / E_L$ is the relative amplitude between the reflection from the lens and the compensating mirror, which can be adjusted by slightly rotating the compensating mirror. Compensation can occurs if $E_L = E_C \quad \phi_C = \pi$, and introducing this condition into (1) yields to:

$$S_{comp}^2 = E_S^2 + E_F^2 + 2E_S E_F \cos(\phi_S - \phi_F) \tag{4}$$

This shows only the signal from the sample that may have an interference pattern generated by the inference between the reflection from the surface and the first surface. However, SOFI samples show little surface reflection so that $E_F = 0$ and $\phi_F = 0$ so the pattern may not be caused because of the interference between these two reflections. Thus, the interference may come from the interference with the reflection of the lens or the compensating mirror.

It is almost impossible to ensure condition (3) because the detector has a background noise (S_0) and equation (3) can be modified as:

$$E_L^2 \left(1 + \alpha^2 + 2\alpha \cos(\phi_C)\right) = S_0^2 \tag{5}$$

This background is small and (5) can be considered as a perturbation of (3). Thus, if $\phi_C = \pi$ is kept constant, then:

$$(\alpha - 1)^2 = \frac{S_0^2}{E_L^2} \tag{6}$$

And equation (4) becomes:

$$\begin{aligned} S_{comp}^2 &= E_S^2 + E_F^2 + 2E_S E_F \cos(\phi_S - \phi_F) + \\ &+ S_0^2 + 2E_L(1-\alpha)[E_S \cos\phi_S + E_F \cos\phi_F] \end{aligned} \tag{7}$$

Another perturbation is to consider $\alpha = 1$ and change the phase:

$$\cos(\pi + \Delta\phi_C) = \frac{S_0^2}{2E_L^2} - 1 \quad \Rightarrow \quad \Delta\phi_C \approx -\frac{S_0^2}{2E_L^2} \tag{8}$$

And then, assuming that the phase is perturbed, equation (4) becomes:

$$\begin{aligned} S_{comp}^2 &= E_S^2 + E_F^2 + 2E_S E_F \cos(\phi_S - \phi_F) + \\ &+ S_0^2 + 2E_L E_S \Delta\phi_C[\cos\phi_S - \sin\phi_S] + 2E_L E_F \Delta\phi_C[\cos\phi_F - \sin\phi_F] \end{aligned} \tag{9}$$

Any of these two perturbations cause the presence of a interference pattern generated by the phase difference of the beam coming from the sample ϕ_S. This phase may be different at each point of the picture because the substrate may not be completely flat or perfectly perpendicular to the optical axis of the system, thus, a small difference of the distance between the substrate and the lens may exist. This pattern is small and can be considered as a background noise of the system. However, if the reflection of from the sample is small because the sample is very thick or highly absorbent, then the pattern is comparable to the signal carrying the defects information and both features appears in the image.

Carbon fiber composites

Both CW and TDS measurements reveal information that are related to the degree of heat damage of the samples. The grid structure of the sample due to the fiber's orientation generated a reflectivity that is highly polarization sensitive of the incoming radiation. The distortion or damage of this grid structure due to the heat changes the local reflectivity and provides the mechanism to get this information with THz waves. In particular, the reflectivity is higher when the radiation's electric field is parallel to the grid and lower when it is perpendicular. Moreover, data obtained with the electric field parallel to the grid shows mainly information about the surface, while the perpendicular field data penetrates deeper into the sample and gets information of the inner layers.

Fig. 5 shows the results of the CW imaging, where it can be seen that the reflectivity of the samples is strongly dependent on the polarization of the incident radiation. The sample shown in Fig. 5-(a) has superficial burn damage that did not result in a significant loss of strength. In the optical image, this damage is apparent, but this is not the case in the THz images, where mainly the structure underneath the top resin layer is observed. Fig. 5-(b) shows a large contrast in the THz image due to the severity of the damage and the perpendicular polarization image provides

a more detailed picture of the structure. Fig. 5-(c) shows a sample with damage confined to a small spot, which shows a high contrast with the undamaged portions of the sample. The structure of the samples allows modeling the reflectivity as a wire-grid polarizer and the reflectivity may be expressed as:

$$R = R_G \cos^2 \theta_P + R_B \tag{10}$$

R_G describes the polarization-sensitive reflectivity of the fiber grid and R_B describes the background reflectivity of the sample, which arises from the fact that the fibers are not entirely unidirectional and are densely spaced in a dielectric resin. These two parameters can be extracted via measurements at orthogonal polarizations and they can give indications of the severity and nature of the damage. For instance, a significant reduction of R_G indicates that there is damage to the fibers (through reorientation or a chemical change) resulting in lower conductivity, while a reduction of R_B can attributed to damage to the resin, conductivity loss, or increased surface roughness.

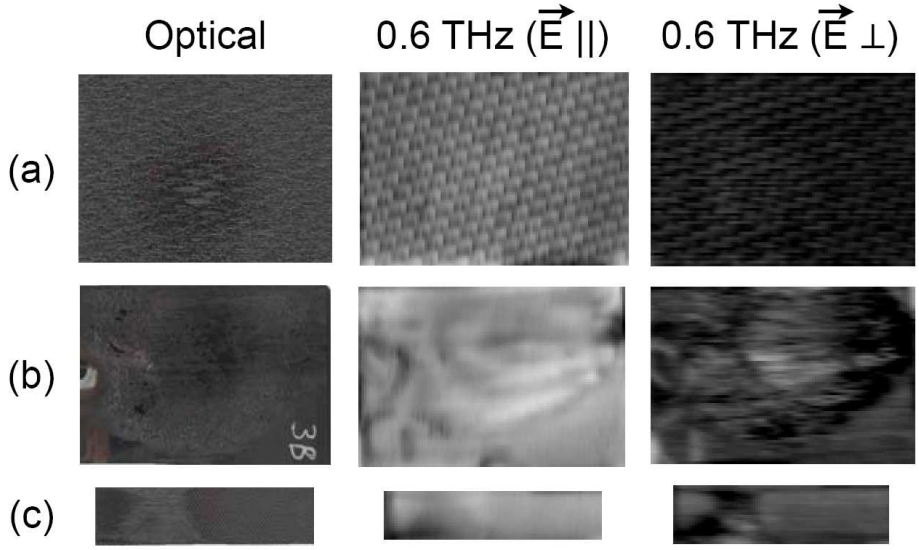

Fig. 5. CW imaging result at 0.6 THz. The first column shows an optical scan of the samples. The second and third columns show the THz images with the (linear) polarization of the beam parallel and perpendicular to the direction of the graphite fibers respectively. (a) sample with superficial burn damage confined to a small spot, (b) sample with broad, severe burn damage across the surface, and (c) sample with severe damage confined to a small spot.

Measurements with THz TDS provide additional information about the material. It is possible to extract the presence and depth of multiple reflections from the surface because this technique is time-resolved. The location of the reflections from different layers can be extracted in the time domain by deconvolving the reflected waveform by a suspect location with a waveform from an undamaged location [11-15]. This information can yield a description of important types of material deformation such as delamination, where multiple layer reflections become separated from one another. Fig. 6 shows examples of THz TDS waveforms from a damaged and undamaged sample surface. There is a clear double-peak structure in the waveform reflected by

the damaged surface, indicating delamination (Fig. 6-(b) and Fig. 6-(e)), which position (Fig. 6-(c) and Fig. 6-(f)) can be obtained by deconvolution. Fig. 6-(a) and Fig. 6-(d) show the load versus displacement that provides information about the mechanical properties of the material. The rising slope of the plot indicates the rigidity of the structure, while the height of the graph indicates the overall strength of the sample. Jagged edges indicate successive failures of layers within the sample. There is a correlation between these mechanical characterization and the THz data in which the more severe the damage is, the more distorted the THz data is from an unburned sample [16].

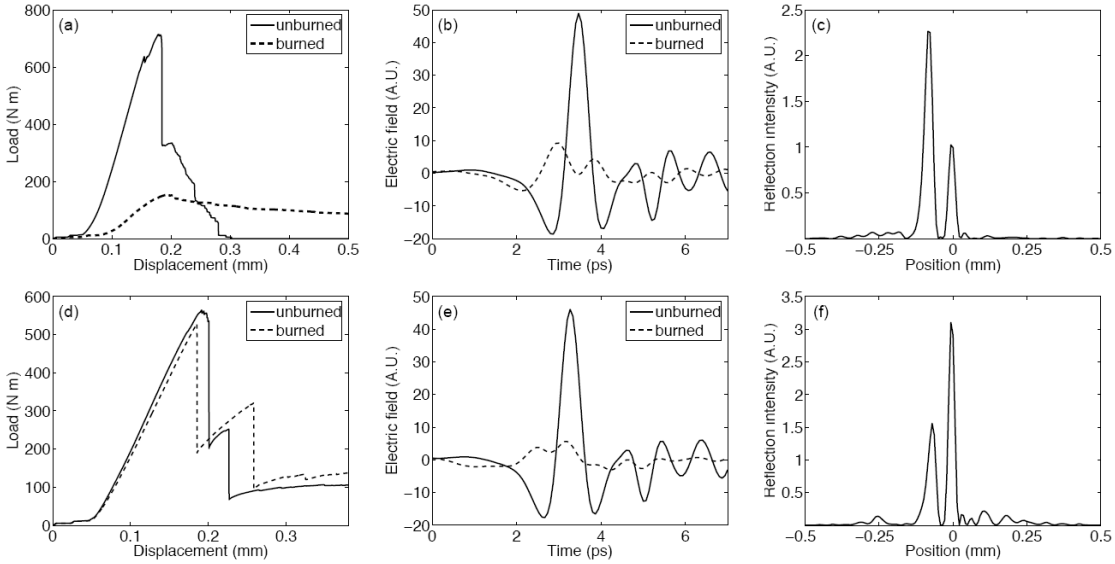

Fig. 6. (a) Load versus displacement characteristics for a two graphite fiber composites of the same kind, one burned (Fig. 5-(b)) and another unburned. (b) THz time-domain waveforms reflected from the surface of these samples. (c) Result of a deconvolution of the waveform from the damaged sample with a reference waveform from the undamaged sample. (d) Load vs. displacement characteristics for a different pair of samples. (e) THz waveforms reflected from their surfaces. (f) Result of a deconvolution of the waveform from the second damaged sample with a reference waveform from the second undamaged sample.

Discussion and conclusion

THz imaging technology has proven to be a very valuable tool in SOFI inspection and has passed NASA's selection criteria in all phases so far. Actually, THz imaging technology and back-scattered X-ray are considered to become space certified in the last test phase. In particular, CW imaging systems are very attractive since they can be compact and easy to operate. However, the presence of the interference pattern in the normal reflection geometry may reduce the detection capabilities especially in thick samples. This problem may be solved by implementing small angle reflection geometry but this will increase the size of the system and reduce the resolution.

In the carbon fiber composites both THz imaging and spectroscopy turn to be a promising solution to the problem of identifying and evaluating the presence of damage or defects and

potentially increase safety and efficiency in the defense and aerospace industries. In all cases, the resolution of the images is enough to detect the most important defects and the false rate calls is reduced because the images are easy recognizable to human vision.

However, additional progress must be done to implement THz as effective tool. For instance, real-world application of these techniques requires speed as well as specificity. So far, the examples shown in this paper utilize a raster scanning technique to form the images, wherein a THz beam is focused and scanned across the sample. This modality is time-consuming and not very attractive for large-scale applications where time is an issue. For these cases, the availability of THz camera would be more attractive and some steps have been taken in this direction for both pulsed and CW THz techniques. For CW THz systems, detector array options include commercially available arrays of pyroelectric detectors, which suffer from high noise-equivalent power, and micro-bolometer arrays, which have been shown to produce usable, real-time imaging combined with quantum cascade lasers [17]. Combined with appropriate optics such detector arrays can be readily adapted to these applications.

Acknowledgements

The inspection of SOFI sample is supported by NASA and Lockheed Martin Space Systems. The authors would like to thank Warren Ussery, Ron Reightler, Eric Madras, James Walker, William Winfree and Frank Helpburn for the foam samples and support.

The inspection of carbon fiber is based upon work supported by the National Science Foundation under Grant No. 0333314. The authors thank Xu Xie, Hua Zhong, Michael Shur and Nezih Pala for technical assistance and David Dawes and Mark J. Perry for providing the samples, mechanical characterization and helpful discussions.

References

1. B.B. Hu, and M.C. Nuss, “Imaging with terahertz waves”, *Opt. Lett.* **20**, 1716 (1995).
2. T.S. Hartwick, D.T. Hodges, D.H. Barker, and F.B. Foote, “Far Infrared Imagery”, *Appl. Opt*. **15**, 1919 (1976).
3. T. Kleine-Ostmann, P. Knobloch, M. Koch, S. Hoffmann, M. Breede, M. Hofmann, G. Hein, K. Pierz, M. Sperling, and K. Donhuijsen, “Continuous-wave THz imaging”, *Electron. Lett.* **37**, 1461 (2001).
4. K. Siebert, H. Quast, R. Leonhardt, T. Löffler, M. Thomson, T. Bauer, and H.G. Roskos, “Continuous-wave all-optoelectronic terahertz imaging”, *Appl. Phys. Lett.* **80**, 3003 (2002).
5. A. Dobroiu, M. Yamashita, Y.N. Ohshima, Y. Morita, C. Otani, and K. Kawase, “Terahertz imaging system based on a backward-wave oscillator”, *Appl. Opt.* **43**, 5637 (2004).
6. J. Xu, H. Zhong, T. Yuan, X. Xu, X.-C. Zhang, R. Reightler, and E. Madras, “T-rays identify defects in insulating materials”, CLEO, CMB2, Washington DC, 2004.
7. “NASA’s implementation plans for space shuttle return to flight and beyond”, vol. 1, Rev. 2, April 26th (2004).

8. N. Karpowicz, H. Zhong, C. Zhang, K.-I Lin, J.-S. Hwang, J. Xu, and X.-C. Zhang, "Compact continuous-wave sub-terahertz system for inspection applications", *Appl. Phys. Lett.* **86**, 054105 (2005).
9. A. Redo, N. Karpowicz, X. Li, and X.-C. Zhang, "Sensing and Imaging with Continuous-Wave Terahertz Systems", *AIP Conference Proceedings* **820**, 1, pp. 508-514 (2006)
10. B. Ferguson, and X.-C. Zhang, "Materials for terahertz science and technology", *Nature Materials* **1**, 26 (2002).
11. R.A. Cheville, and D. Grischkowsky, "Time domain terahertz impulse ranging studies", *Appl. Phys. Lett.* **67,** 1960 (1995).
12. D.M. Mittleman, S. Hunsche, L. Boivin, and M. C. Nuss, "T-ray tomography", *Opt. Lett.* **22**, 904 (1997).
13. T. Dorney, W.W. Symes, R.G. Baraniuk, and D. Mittleman, "Terahertz multistatic reflection imaging", *J. Opt. Soc. Am. A*, **19**, 1432 (2002).
14. D.M. Mittleman, M. Gupta, R. Neelamani, R.G. Baraniuk, J. V. Rudd, and M. Koch, "Recent advances in terahertz imaging", *Appl. Phys. B,* **68,** 1085 (1999).
15. K. McClatchey, M.T. Reiten, and R. A. Cheville, "Time resolved synthetic aperture terahertz impulse imaging", *Appl. Phys. Lett.*, **79**, 4485 (2001).
16. N. Karpowicz, D. Dawes, M.J. Perry, and X.-C. Zhang, "Terahertz characterization of fire damage to carbon fiber materials", *Appl. Phys. Lett.* (submitted).
17. A.W. Lee, and Q. Hu, "Real-time, continuous-wave terahertz imaging by use of a microbolometer focal-plane array", *Opt. Lett.* **30**, 2563-2565 (2005).